Journal of Applied Electrochemistry (2021) 51:411–423
https://doi.org/10.1007/s10800-020-01514-0

RESEARCH ARTICLE

Structural, transport, thermal, and electrochemical properties of $(La_{1-x}Sr_x)_2CoO_{4\pm\delta}$ cathode in solid-oxide fuel cells

Fushao Li[1] · Yingxian Xu[1] · Deqiang Zhao[2] · Long Jiang[3] · Qingqing Wu[1] · Hujun Shen[1] · Mingsen Deng[1]

Received: 30 June 2020 / Accepted: 7 December 2020 / Published online: 6 January 2021

Abstract

Layered perovskite $(La_{1-x}Sr_x)_2CoO_{4\pm\delta}$ ($x=0.3$, 0.4, 0.5) oxides were prepared using sol–gel route and evaluated as the cathode materials for intermediate-temperature solid-oxide fuel cells. $(La_{1-x}Sr_x)_2CoO_{4\pm\delta}$ has a tetragonal structure with space group of *I4/mmm* in all cases of x levels. The average thermal expansion coefficient of $(La_{1-x}Sr_x)_2CoO_{4\pm\delta}$ is relatively low and slightly increases with x, which can be ascribed to the sway of Sr doping on the spin-state transition of Co ions. X-ray photoelectron spectroscopy and thermogravimetric analysis show that Co ions exist in mixed oxidation states, but the lattice oxygen content considerably varies with x. Regarding transport property, $(La_{1-x}Sr_x)_2CoO_{4\pm\delta}$ behaves like a semiconductor in the temperature range of 200–800 °C, and the electrical conductivity significantly increases with x. As one of the most important results, electrochemical performance of $(La_{1-x}Sr_x)_2CoO_{4\pm\delta}$ cathode is affected by x in a complex manner, and $x=0.4$ cathode, i.e., $La_{1.2}Sr_{0.8}CoO_{4\pm\delta}$, has the most favored area-specific resistance of 0.062 Ω cm^2 and the highest power density of 630 mW cm^{-2} in an electrolyte-supported single cell at 800 °C, showing a rapid kinetics toward oxygen reduction reaction. This study demonstrates that the structural, transport, thermal, and electrochemical properties of $(La_{1-x}Sr_x)_2CoO_{4\pm\delta}$ cathodes significantly depend on the La/Sr ratio at the A-site of lattice.

✉ Fushao Li
lifushao@126.com

✉ Hujun Shen
hujun.shen@gznc.edu.cn

✉ Mingsen Deng
deng@gznc.edu.cn

[1] Institute of Advanced Materials and Guizhou Provincial Key Laboratory of Computational Nano-Material Science, Guizhou Education University, Guiyang 550018, Guizhou, China

[2] Key Laboratory of Hydraulic and Waterway Engineering and National Engineering Research Center for Inland Waterway Regulation, School of River & Ocean Engineering, Chongqing Jiaotong University, Chongqing 400074, China

[3] School of Physics and Optoelectronic Engineering, Yangtze University, Jingzhou 434023, Hubei, China

Graphic abstract

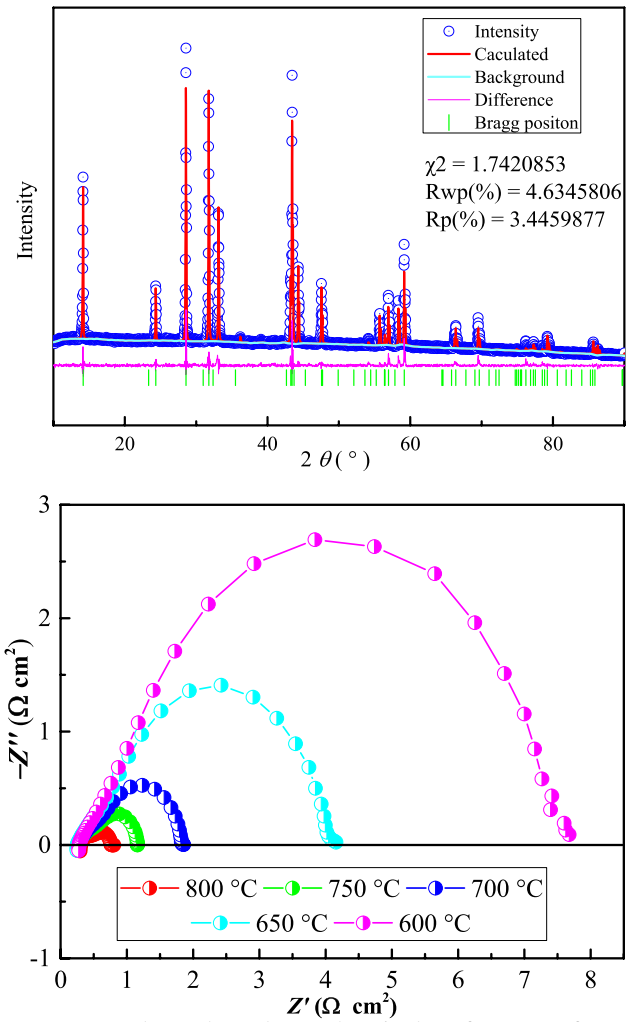

Rietveld refinement profile and temperature-dependent electrochemical performance for $La_{1.2}Sr_{0.8}CoO_{4\pm\delta}$ cathode material

Keywords Solid-oxide fuel cells · Cathode · Electrochemical performance · Oxygen reduction reaction · Area-specific resistance

1 Introduction

Layered perovskite oxides with K_2NiF_4-type structure have attracted considerable interest because of their versatile properties exhibited by different elemental compositions in this structure type, including complex magnetic phenomena, ferroelectricity, superconductivity, catalysis, and mixed ionic-electronic conductivity (MIEC) to mention a few [1, 2]. MIEC, in particular, is a quite utilitarian property for many high-temperature electrochemical applications [3–11]. The ideal K_2NiF_4 structure of layered perovskite oxides can be viewed as an alternative stacking of perovskite-type layers and rock-salt-type layers along *c*-axis [12, 13]. These oxides can accommodate a significant amount of hyperstoichiometric oxygen in interstitial positions in the rock salt layers of the structure owing to their unique way of atomic package [14]. As a mixed ionic-electronic conductor, ionic oxygen conduction in K_2NiF_4-type oxides occurs via a vacancy migration mechanism in the perovskite layers or through the diffusion of interstitial oxygen in the rock salt layers, whereas the electronic conduction behavior originates from the *p*-type electronic conductivity in the perovskite layers [15, 16].

These interesting properties of K_2NiF_4-type oxides have attracted much attention owing to their potential application as cathode materials for intermediate-temperature solid-oxide fuel cells (IT-SOFCs) [17–19]. The rationale for this application is that the speed of oxygen reduction reaction (ORR) on the cathode side can be improved by replacing the triple phase boundary (TPB) of electrolyte-cathode-air

zone with a double interphase boundary of electrolyte-air in the range of intermediate temperature [20, 21]. These compounds also exhibited relatively high oxygen diffusion and surface exchange coefficients, two vital factors governing cathode performance [22, 23].

A functional cathode layer is an important component in SOFCs. Especially in the temperature range of IT-SOFCs, the overall performance of a single cell is significantly restrained by the catalytic activity of an applied cathode, and in many circumstances, ORR on the cathode can even become the most critical rate-limiting step and thus contribute a great deal to a cell's global impedance [24]. Nowadays, a significant progress has been made in reducing polarization loss on the cathode side by applying the ABO_3-type cobaltate perovskite or $A_2B_2O_6$-type double perovskite as the cathode materials for IT-SOFCs, such as $La_{1-x}Sr_xCoO_{3-\delta}$, $Ba_{1-x}Sr_xCo_{1-y}Fe_yO_{3-\delta}$, $Sr_{1-x}RE_xCoO_{3-\delta}$ (RE = rare earth metal), $REBaCo_2O_{5+\delta}$, and their derivatives [25–30]. These materials remarkably outperform the conventional high-temperature counterparts, typically $La_{1-x}Sr_xMnO_3$ [31, 32], because of their prominent electrocatalytic activity and excellent electrical conductivity. However, the thermal expansion coefficients (TECs) of these compounds are usually rather large, making them poor "weldable" and compatible compared with the most commonly used solid-oxide electrolytes [33] such as $Y_{2x}Zr_{1-2x}O_{2-x}$ (YSZ), $Ce_{1-x}Sm_xO_{2-\delta}$ (SDC), and $La_{1-x}Sr_xGa_{1-y}Mg_yO_{3-\delta}$ (LSGM). In contrast, K_2NiF_4-type structural materials have a better thermal stability and more acceptable TECs ($10.5–14.2\times10^{-6}$ K^{-1}) [34–36]. Therefore, K_2NiF_4-type structure of A_2BO_4 materials dominates as the promising cathode candidate for IT-SOFCs.

The most extensively studied systems for such applications are Ln_2NiO_4 (Ln = La, Pr, Nd) [37, 38], typically La_2NiO_4. However, the unique role of redox couple and superior valence variability of cobalt element in ORR is frequently unmatchable relative to other congeners or heteroatoms. Therefore, La_2CoO_4-related oxides are more eligible cathode candidates of IT-SOFC in terms of ORR activity, transport property, etc. Hu and Ghorbani-Moghadam reported that $La_{2-x}Sr_xCoO_4$ series could be applied as promising cathodes for IT-SOFCs after evaluating their thermal stability and conduction properties [39, 40]. They also demonstrated that the electrochemical performance of single-phase cathodes was inferior to $Ln_{2-x}Sr_xCoO_4$-CGO composites. Jin and Liu studied $Ba_{1.2}Sr_{0.8}CoO_4$-GDC composite cathodes and found that the performance of composite cathode was greatly enhanced [41]. Zhou and Chen also confirmed that $La_{0.8}Sr_{1.2}CoO_4$-CGO composite cathode exhibited much improved performance compared with the corresponding single-phase cathode [42].

Although $(La,Sr)_2CoO_4$-electrolyte composite cathodes present favorable electrochemical performance in contrast to $(La,Sr)_2CoO_4$ single-phase compounds, its practical application is still questionable because of many problems such as compositional compatibility, long running stability, and inconvenient preparation route. In this sense, the single-phase cathode material is often considered preferentially, provided that its key electrochemical activity is sufficient and other properties are well balanced. Moreover, the effect of Sr doping on the underlying structure and intrinsic properties of $(La,Sr)_2CoO_4$ still lacks in-depth investigation and detailed interpretation against a background of SOFCs, and the electrochemical performance with Sr-doping content is far from optimization. Roughly speaking, aliovalent A-site doping will inevitably induce changes in crystal field structure and transport property and in turn affect the electrochemical performance. Tealdiet al. studied the transport properties of $La_{2-x}Sr_xCoO_4$ solid solution and found that $La_{0.8}Sr_{1.2}CoO_4$ has the best electrical conductivity in the entire temperature range (300–750 °C) [43]. However, their conclusions are essentially drawn from the density functional theory calculation, and the preliminary conditions are highly hypothetical. Electrochemical performance with this composition still needs to be evaluated.

In this study, we designed and prepared $(La_{1-x}Sr_x)_2CoO_{4\pm\delta}$ compounds with high Sr-doping level ($x = 0.3, 0.4, 0.5$) to serve as single-phase cathode materials for IT-SOFCs. We believe that a change in Sr-doping content can effectively alter oxygen diffusion and surface exchange by modifying the crystal field and by tuning the electronic structure. Therefore, the effect of x value on the structure, oxygen content, thermal expansion, and electrochemical performance was systematically investigated.

2 Experimental

2.1 Cell fabrication

As preliminary materials, $(La_{1-x}Sr_x)_2CoO_{4\pm\delta}$ polycrystalline powders were prepared via sol–gel route. First, stoichiometric amounts of $La(NO_3)_3{\cdot}6H_2O$, $Sr(NO_3)_2$, and $C_4H_6O_4Co{\cdot}4H_2O$ (cobalt acetate) were dissolved into a minimum volume of deionized water, and ethylenediaminetetraacetic acid (EDTA) and anhydrous citric acid were added. The molar ratio of total metal ions to citric acid and EDTA was set as 1:2:1. An aqueous solution of NH_3 was then used to adjust the solution pH to ~ 8. This salt solution was then placed on a heated plate for drying till a homogeneous gel was obtained. The gel was further completely dried in an oven at 150 °C for many hours, decomposed at 450 °C for 5 h, and annealed at 900–1300 °C for 10–20 h in an air furnace after thoroughly grinding the decomposed intermediate products. Other materials such as $La_{0.8}Sr_{0.2}Ga_{0.83}Mg_{0.17}O_{2.815}$ (LSGM) dense electrolyte

discs and $Ce_{0.8}Sm_{0.2}O_{1.9}$ (SDC) fine powders were prepared via solid-state reaction, as described in our previous studies [44, 45].

Button-type cells were fabricated into the electrolyte-supported type, where $(La_{1-x}Sr_x)_2CoO_{4\pm\delta}$ cathodes were simply constructed by sintering the precursor layer on the LSGM disc (300 ± 10 µm thick) at 1050 °C (roughly optimized temperature) for 5 h in air. The precursor layer was screen-printed with a slurry containing ethylcellulose. This slurry was essentially made of $(La_{1-x}Sr_x)_2CoO_{4\pm\delta}$ fine powders after the ball-milling (2 h, 330 rpm) of the as-prepared preliminary samples (10 h annealing, 1000 °C), thus reducing $(La_{1-x}Sr_x)_2CoO_{4\pm\delta}$ grains to uniform particles. The anode structure was constructed following our previous studies [46, 47]. Routinely, the anode (*ca*. 30 µm thickness) was constructed before the cathode by screen-printing "NiO-SDC'' slurry onto SDC buffer layer (*ca*. 10 µm thickness) and subsequently baking at 1250 °C for 4 h, whereas the SDC buffer layer was prepared by screen-printing SDC slurry onto LSGM disc and sintering at 1300 °C for 2 h in air. Note that the anode is composed of thoroughly ball-milled 65 wt% NiO nanoparticles and 35 wt% SDC fine powders.

2.2 Characterization and test

The crystal structure of $(La_{1-x}Sr_x)_2CoO_{4\pm\delta}$ was determined by X-ray powder diffraction (XRD, Rigaku: Ultima IV) in Bragg–Brentano reflection geometry with Cu Kα radiation at 40 kV and a receiving slit of 0.2–0.4 mm. The diffraction patterns were collected at room temperature (RT) by step scanning in the range of $10° \le 2\theta \le 90°$ with a scan rate of $5°\ min^{-1}$. The structural parameters were refined using the Maud software and Rietveld method. The micromorphological structure of samples was observed using a field-emission scanning electron microscope (FSEM, ZESS: Sigma 300), and the electron acceleration voltage was 20 kV. The binding state of compositional elements in $(La_{1-x}Sr_x)_2CoO_{4\pm\delta}$ was analyzed using an X-ray photoelectron spectrometer (XPS, ThermoFisher Scientific: EscaLab 250Xi). The incident radiation was monochromatic Al Kα X-rays (1486.6 eV). Narrow high-resolution scans were run to obtain O1s and Co2p level spectra with 0.05 eV steps. All binding energies were referenced to the C1s peak (285 eV) arising from adventitious carbon.

The oxygen loss under thermal impact was measured by thermogravimetric analysis (TGA, METTLER TOLEDO: TGA2) carried out under ambient pressure from RT to 900 °C. The amount of sample powder was ~ 15 mg, and the heating rate was 5 °C min^{-1}. A linear thermal expansion test was carried out on rectangular bar specimens ($5 \times 5 \times 25$ mm^3) by using a dilatometer (NETZSCH: DIL 402C); the heating program ranged from RT to 1000 °C at a running rate of 5 °C min^{-1}. Electrical conductivity was measured with disc specimens using a four-probe tester (Suzhou Jingge: ST2253); Ag wire and Ag paste were used to make the four probes. To prepare two types of these specimens, the as-prepared preliminary $(La_{1-x}Sr_x)_2CoO_{4\pm\delta}$ samples (10 h of annealing, 1000 °C) were ball-milled (2 h, 330 rpm) and then pressed into molds under a pressure of 100 MPa, followed by sintering at 1300 °C for 20 h to full densification in an air furnace.

Electrochemical performance was measured using an advanced electrochemical system (Princeton Applied Research: PARSTAT 2273). Electrochemical impedance spectroscopy (EIS) across symmetrical "cathode|LSGM|cathode" cells was carried out around open circuit voltage (E_{OCV}) using a voltage disturbance signal of 10 mV amplitude, and the frequency was modulated from 100 kHz to 10 MHz. Current–potential (*I–V*) profiles as well as current–power (*I–P*) curves were measured on a single cell to demonstrate the power density output and polarization extent.

3 Results and discussion

3.1 XRD

Figure 1a shows the XRD patterns of $(La_{1-x}Sr_x)_2CoO_{4\pm\delta}$ polycrystalline powders resulting from 20 h of thorough annealing at 1300 °C. All diffractions are well indexed to the K_2NiF_4 structure, and its crystallographic package is shown in Fig. 1b, indicating that this lattice exhibits much tolerance with a high level of Sr substitution. In the crystal structure, the lattice robustness of $(La_{1-x}Sr_x)_2CoO_{4\pm\delta}$ heavily depends on the perovskite-type layers since $(La_{1-x}Sr_x)_2CoO_{4\pm\delta}$ can be reformulated as $La_{1-x}Sr_xCoO_3 \bullet La_{1-x}Sr_xO \bullet O_{\pm\delta}$ according to its atomic arrangement (Fig. 1b). To assess this structural stability, we calculated the Goldschmidt tolerance factor *t*, defined by

$$t = \frac{r_A + r_O}{\sqrt{2}(r_A + r_B)}, \tag{1}$$

where r_A, r_B, and r_O (140 pm) are the average ionic radii of weighted A, B, and O in ABO_3-type perovskite, respectively [48]. If $t = 1$, the perovskite-type layers present an ideal cubic symmetry. The *t* values were calculated for every Co ion state, and the results are shown in Table 1. The *t* values in all cases are close to 1, indicating that the crystal structure of $(La_{1-x}Sr_x)_2CoO_{4\pm\delta}$ retains a high symmetry despite the incorporation of heavy Sr dopant.

In the crystal structure, another interesting phenomenon was also observed in Fig. 1a. Compared with $x = 0.3$ sample, obvious crystallographic orientation occurred in the other two samples. For instance, the X-ray reflection of some

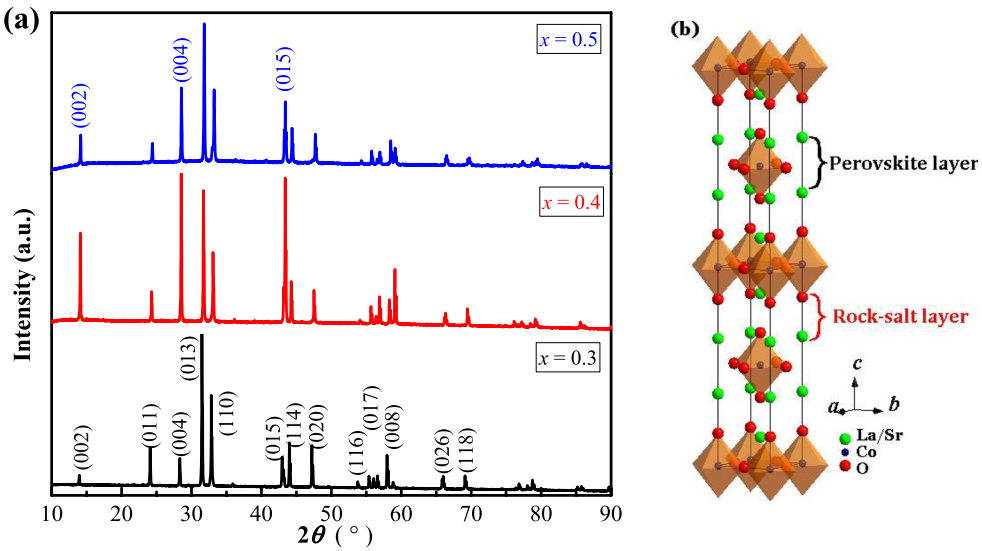

Fig. 1 **a** XRD patterns of $(La_{1-x}Sr_x)_2CoO_{4\pm\delta}$ samples resulting from full annealing at 1300 °C in air for 20 h, **b** crystal structure of tetragonal layered perovskite

Table 1 Summary of average ionic ratios and Goldschmidt tolerance factor *t* for the perovskite-type layers in $(La_{1-x}Sr_x)_2CoO_{4\pm\delta}$ samples

x value	r_A*/pm	r_O/pm	*t* value				
			Co^{2+}(HS)	Co^{2+}(LS)	Co^{3+}(HS)	Co^{2+}(LS)	Co^{4+}
0.3	107.64	140	0.961	1.014	1.038	1.080	1.090
0.4	109.12	140	0.959	1.012	1.035	1.077	1.087
0.5	110.60	140	0.957	1.010	1.032	1.073	1.083

*r_A is average ionic radii of weighted La^{3+} and Sr^{2+} based on molar ratio

crystallized planes was greatly strengthened, such as (002), (004), and (015) planes. Clearly, the kinetics of crystal grain growth under the annealing conditions is greatly influenced by certain levels of Sr doping.

The XRD patterns were further analyzed by Rietveld method using a tetragonal structure with space group *I4/mmm* [49], and the refined profile is shown in Fig. 2. The lattice parameters obtained after executing Rietveld refinement are shown in Table 2. The profile R_p and weighted profile R_{wp} parameters indicate that the refined results are quite reliable and acceptable. Interestingly, the lattice parameters gradually decreased with increasing amount of Sr doping instead, because the size of Sr^{2+} ion (radii 118 pm) is much larger than that of La^{3+} ion (radii 103.2 pm). This can be ascribed to volume contraction due to the loss of lattice oxygen to compensate less contribution of valence electron after the substitution of Sr^{2+} with La^{3+}. Therefore, more amount of oxygen deficiency is expected in $(La_{1-x}Sr_x)_2CoO_{4\pm\delta}$ with a higher level of Sr substitution.

3.2 XPS

The chemical environment of key elements in all $(La_{1-x}Sr_x)_2CoO_{4\pm\delta}$ samples was assessed by XPS, as shown in Fig. 3. The analysis was carried out by the curve-fitting of O 1s and Co 2d spectra because the valence states of Sr^{2+} and La^{3+} ions are stable. In Fig. 3a, the peak nearby 779 eV resulted from Co $2p_{3/2}$ with a shakeup satellite around 789 eV, whereas the peak nearby 794 eV resulted from Co $2p_{1/2}$ with a satellite peak around 803 eV. The presence of these doublets and the obvious satellites near them indicate the coexistence of mixed valences, commonly Co^{3+} and Co^{2+} [50, 51], as confirmed by the two deconvoluted peak components. The O 1 s spectral profile in Fig. 3b can be primarily deconvoluted into two components at around 528 and 530 eV for all samples. The peak at a low binding energy commonly arises from the surface lattice oxygen ($O_{lattice}$: O^{2-}), whereas that at a higher binding energy frequently arises from the adsorbed oxygen ($O_{surface}$: O^-, O^{2-}, or O_2) [52, 53]. However, the ratio of $O_{lattice}/O_{surface}$ substantially differs from each other according to area fraction of each peak, as visually indicated by the guiding scale-lines. According to this ratio, $x = 0.4$ sample contains the maximum amount of lattice oxygen, and we speculate that this may arise from the entry of more oxygen into the interstitial sites. If not so, $x = 0.3$ sample would contain the maximum of lattice oxygen, and $x = 0.5$ sample would contain the minimum of lattice oxygen, because the excess negative charges after the substitution of Sr^{2+} with La^{3+} can only be compensated either

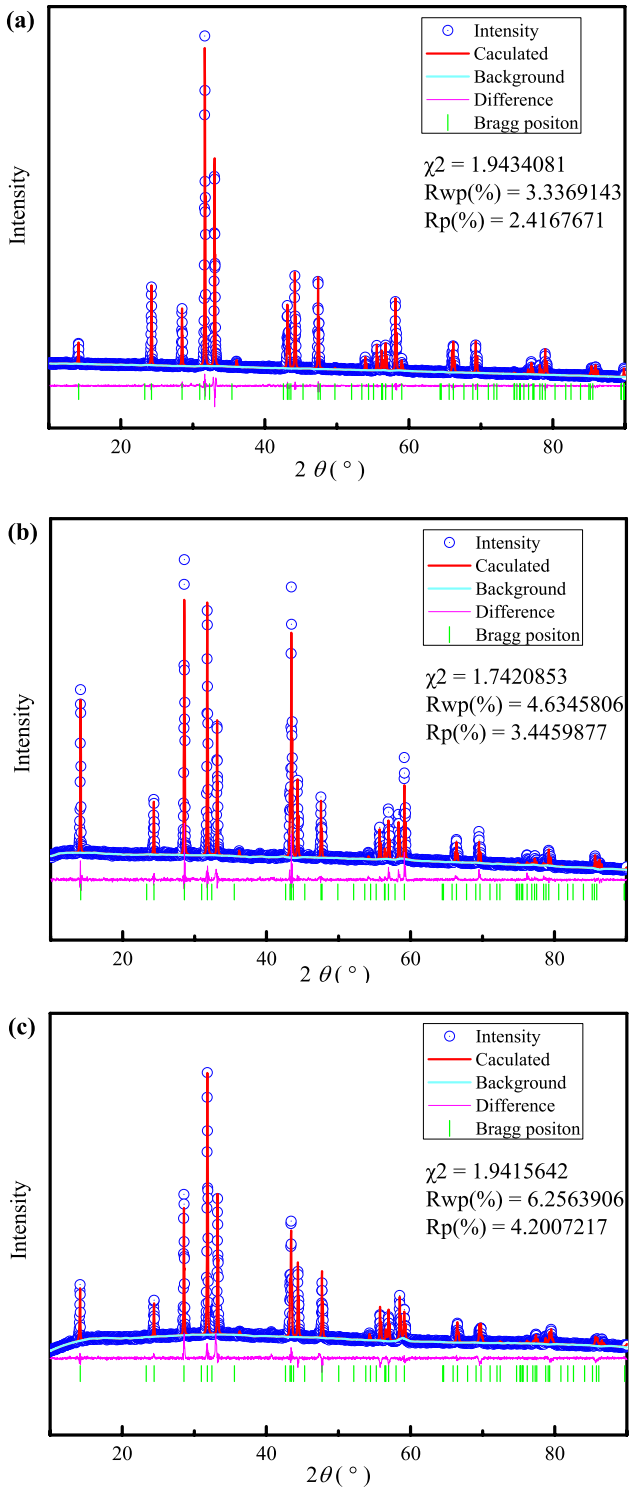

Fig. 2 Rietveld refinement profile for $(La_{1-x}Sr_x)_2CoO_{4\pm\delta}$: **a** $x=0.3$, **b** $x=0.4$, **c** $x=0.5$

by the creation of oxygen vacancies or by the creation of holes, i.e., the oxidation of Co^{2+} to Co^{3+} according to the principle of electroneutrality, as expressed in Kröger–Vink Eqs. (2) and (3).

Table 2 Room-temperature lattice parameters obtained by Rietveld refinement on XRD patterns for $(La_{1-x}Sr_x)_2CoO_{4\pm\delta}$

x value	0.3	0.4	0.5
Space group	*I4/mmm*	*I4/mmm*	*I4/mmm*
a (Å)	3.8328(0)	3.8196(8)	3.8085(1)
c (Å)	12.5146(2)	12.4846(2)	12.4875(4)
c/a	3.2652	3.2686	3.2788
V (Å^3)	191.86(1439)	190.74(1431)	190.23(1427)
χ^2	1.9434081	1.7420853	1.9415642
R_{wp} (%)	3.34	4.63	6.26
R_p (%)	2.42	3.45	4.20

$$SrO + La_{La}^{\times} + Co_{Co}^{\times} + \frac{1}{2}O_2 \rightarrow Sr_{La}' + Co_{Co}^{\cdot} + \frac{1}{2}La_2O_3 \quad (2)$$

$$2SrO + 2La_{La}^{\times} + O_O^{\times} \rightarrow 2Sr_{La}' + La_2O_3 + V_O^{\cdot\cdot}. \quad (3)$$

The presence of oxygen vacancy plays an important role in the conduction mechanism of oxygen ions. In addition to Sr doping, an increased temperature can also lead to the formation of oxygen vacancy. Reduction of high-valence Co ions usually takes place during heating. To counteract this effect, the lattice oxygen is then expelled out, and in turn oxygen vacancies are left behind for $(La_{1-x}Sr_x)_2CoO_{4\pm\delta}$ based on Eq. (4).

$$2Co_{Co}^{\times} + O_O^{\times} \rightarrow 2Co_{Co}' + V_O^{\cdot\cdot} + \frac{1}{2}O_2. \quad (4)$$

3.3 TGA curves

Equation (4) also shows that the weight of sample might change during the formation of oxygen vacancies during heating. For cathode materials, oxygen vacancies are crucial to transfer oxygen ions into the electrolyte, while mixed Co^{3+}/Co^{2+} redox couple produces polaronic conduction for the transfer of electrons. Hence, a TGA operation was carried out between RT and 900 °C under ambient partial pressure of oxygen; Fig. 4 shows the TGA curves for $(La_{1-x}Sr_x)_2CoO_{4\pm\delta}$ samples. A gradual weight loss was observed with increasing temperature for all samples. However, a close comparison reveals that $x=0.4$ sample has the most extent of weight loss. This result further confirms the assumption that more oxygen can enter into the interstitial sites of $x=0.4$ sample as inferred from the O 1s profile. If interstitial oxygen is not involved, the weight loss of oxygen in $x=0.3$ sample would be most obvious according to Eq. (3).

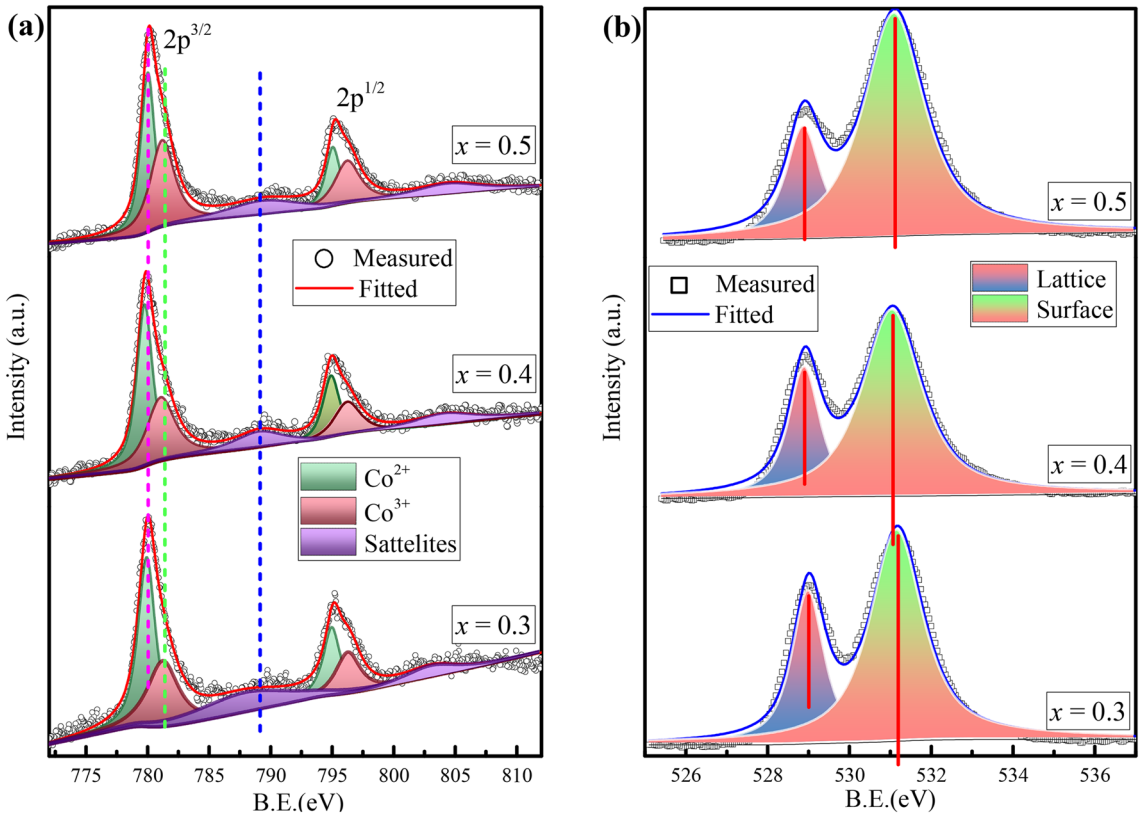

Fig. 3 XPS of the as-prepared $(La_{1-x}Sr_x)_2CoO_{4\pm\delta}$: **a** Co 2p, **b** O 1s

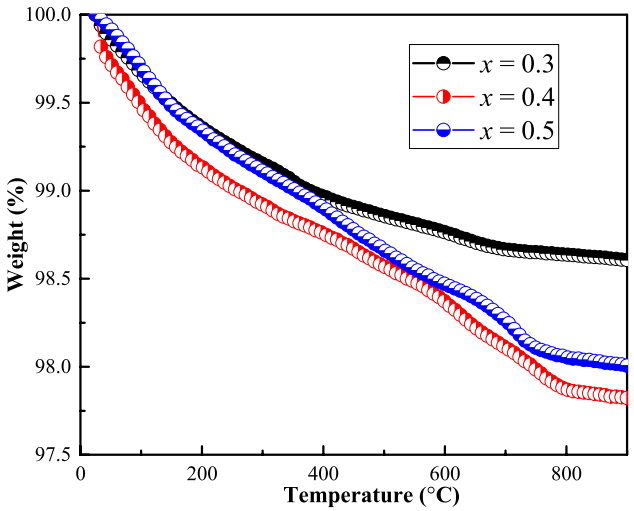

Fig. 4 TGA curves of the as-prepared $(La_{1-x}Sr_x)_2CoO_{4\pm\delta}$ samples

3.4 Electrical conductivity

The oxygen vacancies in the lattice, partial reduction of ions, and generated electronic charge carriers all contribute to the overall transport ability of a mixed conductor. Electrical conductivity (σ) of $(La_{1-x}Sr_x)_2CoO_{4\pm\delta}$ was measured using the four-probe method, and the corresponding results are shown in Fig. 5. The temperature-dependent plots of σ in Fig. 5a show that $(La_{1-x}Sr_x)_2CoO_{4\pm\delta}$ has good transport ability and behaves like a semiconductor. When the temperature was increased from 200 to 800 °C, σ increased from *ca.*1–10 to *ca* 20–120 S cm^{-1}. The σ of $(La_{1-x}Sr_x)_2CoO_{4\pm\delta}$ gradually increases with x values at a fixed temperature, and these specimens follow the order of $x=0.5>x=0.4>x=0.3$. This result is quite natural because acceptor-dopant Sr^{2+} generally enhances the carries density according to Eq. (2) and (3).

From the further Arrhenius plots of lg(σT) vs. 1000 T^{-1} shown in Fig. 5b, $(La_{1-x}Sr_x)_2CoO_{4\pm\delta}$ can hardly be regressed into a straight line in the entire range of temperatures, indicating that more than one transport mechanism is dominant. We assume that the charge transport in $(La_{1-x}Sr_x)_2CoO_{4\pm\delta}$ is not only governed by the transfer of polaronic but also governed by the migration of oxygen ions including the normal lattice ions and interstitial ions. This complexity in transport property is also observed in the analysis of O 1s and TGA of $(La_{1-x}Sr_x)_2CoO_{4\pm\delta}$.

3.5 Thermal expansion

To evaluate the mechanical compatibility of $(La_{1-x}Sr_x)_2CoO_{4\pm\delta}$ with other components of cells, the

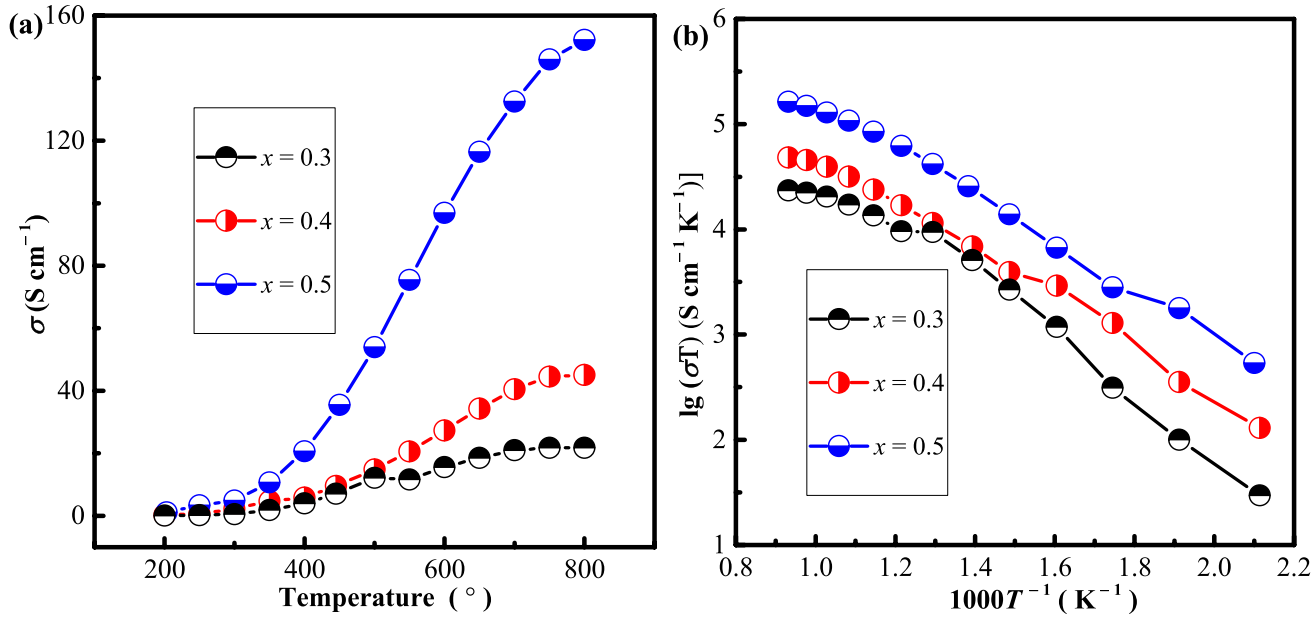

Fig. 5 Electrical conductivity (σ) of $(La_{1-x}Sr_x)_2CoO_{4\pm\delta}$ specimens: **a** temperature dependence of σ, **b** Arrhenius plots of lg(σT) vs. 1000 T^{-1}

TECs were comparatively evaluated by conducting a linear thermal expansion test, as shown in Fig. 6. The plots of linear thermal expansion vs. higher temperatures in Fig. 6a show that the thermal expansion of $(La_{1-x}Sr_x)_2CoO_{4\pm\delta}$ is generally closer to those of typical solid-oxide electrolytes [47]. TECs are simultaneously calculated in Fig. 6b. The TECs for $(La_{1-x}Sr_x)_2CoO_{4\pm\delta}$ samples vary within the range of 6–16 × 10^{-6} K^{-1} from RT to 900 °C, and around 800 °C, the TECs are 14 × 10^{-6} K^{-1}, 15 × 10^{-6} K^{-1}, and 16 × 10^{-6} K^{-1} for the x = 0.3, 0.4, and 0.5 samples, respectively. Interestingly, the TECs of $(La_{1-x}Sr_x)_2CoO_{4\pm\delta}$ above 600 °C decrease with heating temperatures instead, and this phenomenon is worth further investigation.

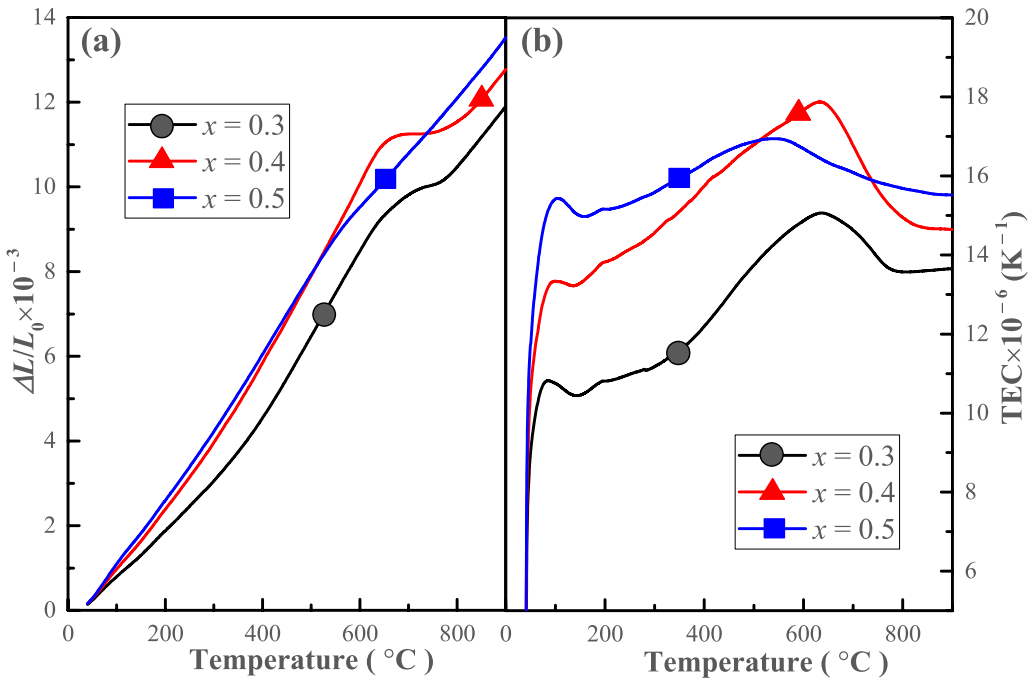

Fig. 6 Thermal expansion of $(La_{1-x}Sr_x)_2CoO_{4\pm\delta}$ specimens: **a** temperature-dependent linear thermal expansion, **b** the corresponding TECs

According to the experiment, incorporation of Sr dopant into the tetragonal lattice of layered perovskite exerts a unique effect on the thermal expansion behavior, and the TECs increased with x values on the whole. In light of the crystal field theory, temperature-dependent transition of spin-state transition and Jahn–Teller distortion of CoO_6 octahedron are the two most primary factors that induce the thermal expansion behavior of cobalt-containing oxides [54, 55]. The Co^{3+} ions in [CoO_6] octahedral can exist in three different spin states, viz. low-spin (LS) state with all 3*d*-electrons in the t_{2g} orbitals, i.e., $t_{2g}^6 e_g^0$, intermediate-spin (IS) state with five electrons in the t_{2g} orbitals, i.e., $t_{2g}^5 e_g^1$, and high-spin (HS) state with four electrons in the t_{2g} orbitals, i.e., $t_{2g}^4 e_g^2$. Therefore, the observed increased TECs of $(La_{1-x}Sr_x)_2CoO_{4\pm\delta}$ with a higher Sr content can be reasonably explained. Because lower-valence Sr^{2+} will strengthen Co–O bond compared with higher-valence La^{3+}, introduction of Sr^{2+} into $La_2CoO_{4\pm\delta}$ lattice frequently leads to a transition from the HS to LS states, as observed in the $LaCoO_{3-\delta}$ with a similar perovskite structure [50]. Moreover, the crystal field of $(La_{1-x}Sr_x)_2CoO_{4\pm\delta}$ can also be modified by the interstitial oxygen ions, which is sensitive to temperature, as discussed on TGA curves. On the other hand, a higher temperature commonly induces a transition of Co ions from the LS to higher-spin state. Therefore, the volume expansion effect due to the transfer of LS state of Co^{3+} ions to HS state during heating is eventually strengthened by Sr doping.

3.6 Electrochemical performance

Electrochemical performance of cathode was studied by EIS across a symmetrical "cathode|LSGM|cathode" cell in air. The kinetics of ORR across $(La_{1-x}Sr_x)_2CoO_{4\pm\delta}$ cathode with different Sr-doping contents was compared in Fig. 7. The Nyquist plot of spectrum shows that the catalytic activity of a cathode is directly correlated with the length of real axes intercepts, commonly designated as the area-specific resistance (*ASR*), and a smaller *ASR* value is equivalent to a faster speed of ORR. The Nyquist plot of Fig. 7a shows that the kinetics of ORR is significantly affected by the dopant of lower-valence Sr ions, and the corresponding *ASR* decreased from 0.095 to 0.062 Ω cm^2 when $x=0.3$ is first increased to $x=0.4$. Then, the *ASR* increased from 0.062 to 0.093 Ω cm^2 when $x=0.4$ is increased to $x=0.5$. Evidently, $x=0.4$ cathode has the highest electrocatalytic activity toward ORR, and our result slightly deviates from other studies [42]. In the Arrhenius plots of ln*ASR* vs. 1000 T^{-1} shown in Fig. 7b, the regression lines show that the activation energies of ORR (E_a) for $x=0.3$, 0.4, and 0.5 cathodes are 134, 131, and 129 kJ mol^{-1}, respectively. Statistically, E_a is slightly

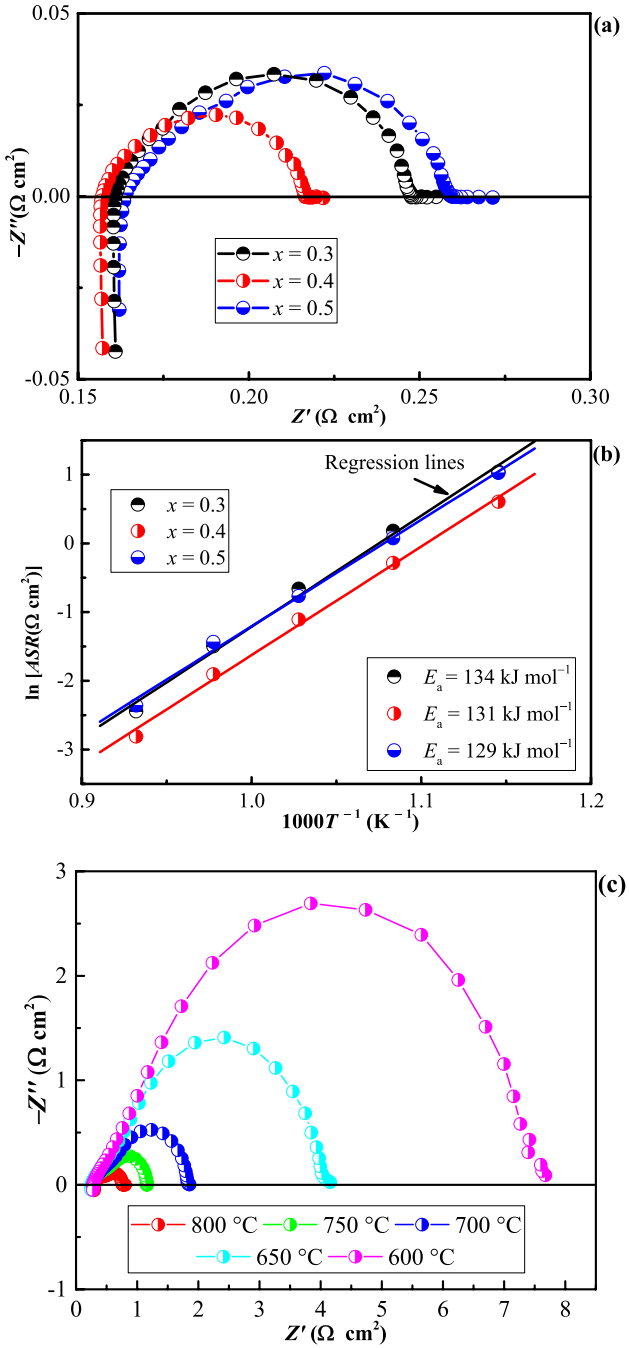

Fig. 7 EIS of $(La_{1-x}Sr_x)_2CoO_{4\pm\delta}$: **a** Nyquist plot at 800 °C, **b** Arrhenius plots of ln*ASR* vs. 1000 T^{-1}, **c** Nyquist plot with $x=0.4$ electrode at different temperatures

changed by x values or Sr-doping contents, demonstrating that the ORR is dominated by the same mechanisms in all cathodes. We speculate that the surface exchange coefficients of $La_2CoO_{4\pm\delta}$ cathode remain almost unchanged even after the entry of lower-valence Sr^{2+} because this parameter

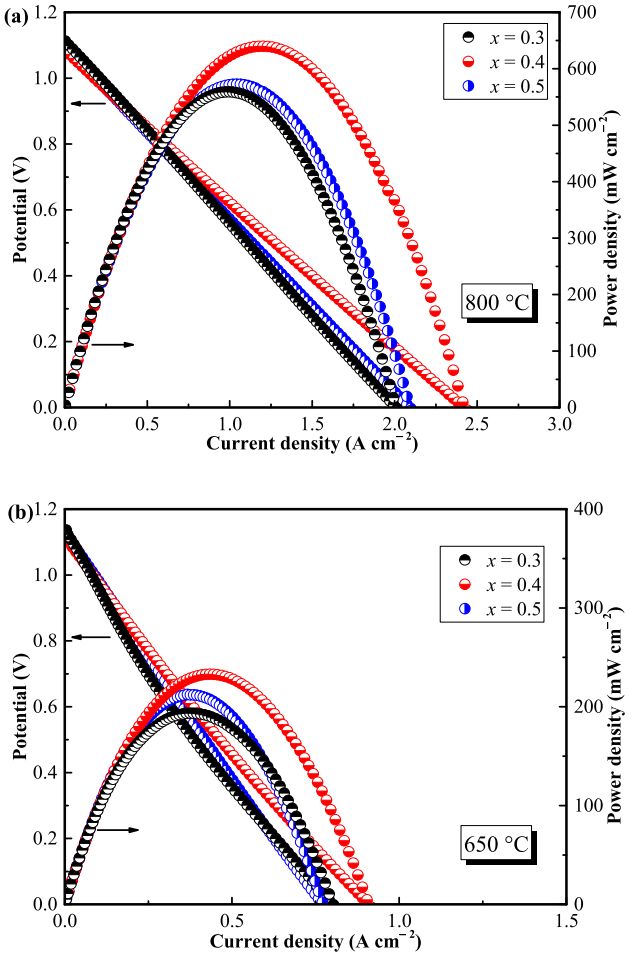

Fig. 8 Cell potential and power density dependence on the current density with $(La_{1-x}Sr_x)_2CoO_{4\pm\delta}$ cathode at **a** 800 °C and **b** 650 °C

is mainly determined by the amount of Co–O bonding ends, but the speed of oxygen diffusion would be significantly influenced by Sr doping, as discussed in the XPS of O 1s and TGA results of $(La_{1-x}Sr_x)_2CoO_{4\pm\delta}$. ORR mechanism is more related to the surface exchange coefficients than oxygen diffusion, but oxygen diffusion can significantly modify the TPB area and then enhance the speed of ORR. Comparatively, temperature significantly affects the kinetics of ORR electrode process, as shown in Fig. 7c where the thermal effect on the evolution of Nyquist plot is exemplified by $x=0.4$ electrode.

The output performance of single cells was tested, and the power density and cell potential as a function of current density at different temperatures are shown in Fig. 8. A single cell was built with $(La_{1-x}Sr_x)_2CoO_{4\pm\delta}$ cathode, Ni-SDC anode, and 300-μm-thick LSGM electrolyte, and pure H_2 flow was fed as the fuel. The open circuit potential reached around 1.10 V even at 800 °C, almost close to the Nernstian extreme. The nearly linear current–potential relationship means that a considerable portion of the potential was consumed by the thick LSGM electrolyte. Despite this adverse effect, the maximum power density of as high as *ca.*630 and 230 mW cm^{-2} at 800 and 650 °C, respectively, was still achieved from $x=0.4$ cathode. This is higher than the other two Sr-doping levels, showing a rapid kinetics toward ORR. This result agrees with the conclusion drawn from EIS investigation.

3.7 Cathode/electrolyte interface

A postmortem analysis of cells was made, and sectional cathode/LSGM interfaces were specially examined by FSEM, as shown in Fig. 9. By comparing the tissue of all cathodes as shown in Fig. 9a, c, e, it was found that all the three types of cathode are firmly connected with LSGM electrolytes, and all the cathode layers produce adequate porosity and sufficient TPBs for ORR. All these structural properties are essential for the stable running of a cathode in the working cells. Further from Fig. 9b, d, f, only a negligible difference is observed between the particle size of cathode grains because of Sr doping. Therefore, the kinetics of ORR is primarily governed by the intrinsic properties of $(La_{1-x}Sr_x)_2CoO_{4\pm\delta}$ rather than the morphological structures.

4 Conclusion

Layered perovskites $(La_{1-x}Sr_x)_2CoO_{4\pm\delta}$ with various La/Sr ratios were readily prepared via sol–gel route and evaluated as cathode materials for IT-SOFCs. The air-annealed $(La_{1-x}Sr_x)_2CoO_{4\pm\delta}$ compounds show the *x*-dependent lattice parameters, and the structure is tetragonal with space group of *I4/mmm* in the range of $0.3\le x\le 0.5$. $(La_{1-x}Sr_x)_2CoO_{4\pm\delta}$ oxides have two different oxygen chemical states and contain mixed Co^{2+}/Co^{3+} ions. A change in Sr-dopant content can effectively tune the lattice structure, interstitial oxygen content, and oxygen vacancy. $(La_{1-x}Sr_x)_2CoO_{4\pm\delta}$ samples have a good electrical conductivity (> 20 S cm^{-1}) at 800 °C, which increases with the elevated temperature and enhanced Sr-doping content. An improved electrochemical performance was obtained by a moderate substitution of Sr^{2+} with La^{3+}, and the $x=0.4$ cathode shows the most favored polarization resistance of 0.062 Ω cm^2 and exhibits the maximum power density of 630 mW cm^{-2} at 800 °C. This study demonstrates

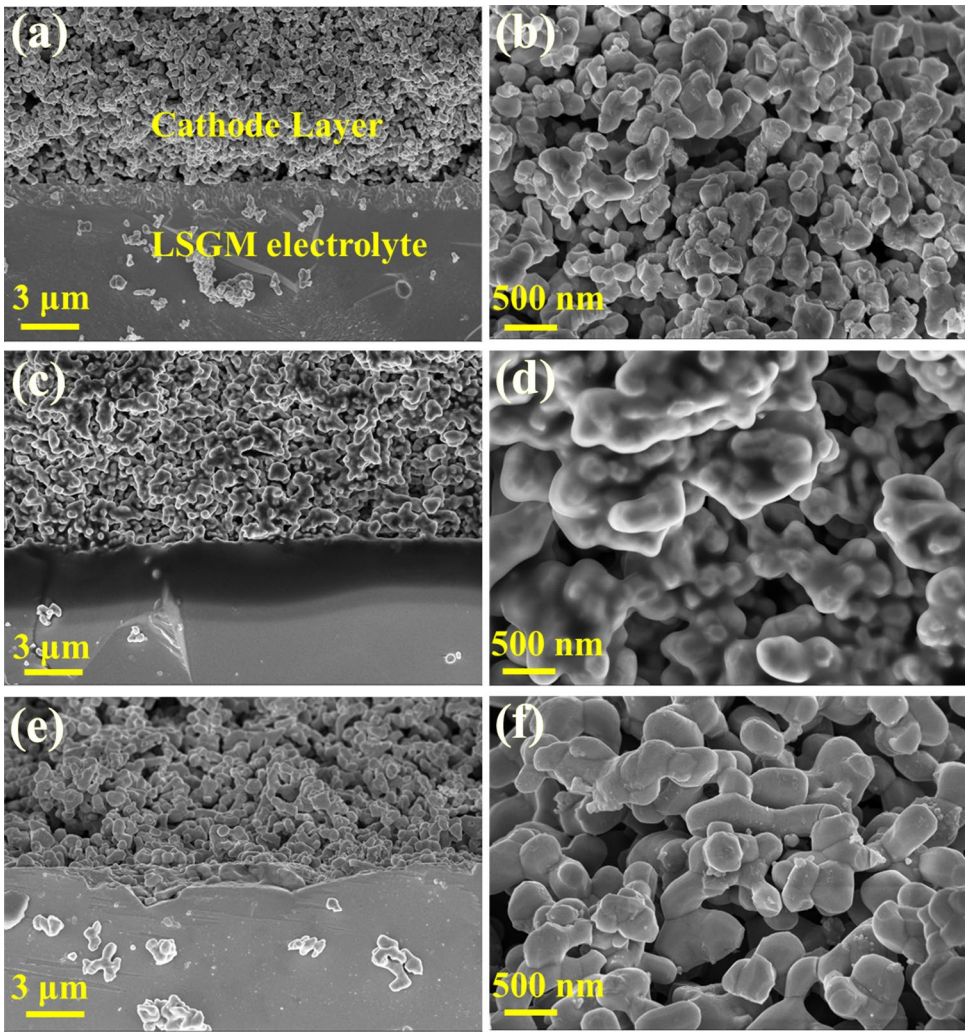

Fig. 9 Sectional $(La_{1-x}Sr_x)_2CoO_{4\pm\delta}$ cathode/electrolyte interface and cathode grain morphology: (**a**, **b**) $x=0.3$, (**c**, **d**) $x=0.4$, (**e**, **f**) $x=0.5$

that layered perovskites $(La_{1-x}Sr_x)_2CoO_{4\pm\delta}$ with mixed ionic and electronic conduction are quite promising cathode materials for IT-SOFCs.

Acknowledgements This study was supported by the Natural Science Foundation of China (Grants 52062006, 21763007, and 21863002) and by the Program for Innovative Research Team of Guizhou Province (QKHPTRC-[2020]5023). The authors would like to thank the Hundred Talents Program of Guizhou Province (No. QKHPTRC[2016]5675) for financial support and acknowledge the Center for Magnetic Materials and Devices of Qujing Normal University for structural characterizations.

References

1. Ram RAM, Ganguly P, Rao CNR, Honig JM (1988) Preparation and characterization of $La_2CoO_{4+\delta}$. Mater Res Bull 23(4):501
2. Goodenough JB (2004) Electronic and ionic transport properties and other physical aspects of perovskites. Rep Prog Phys 67(11):1915
3. Riza F, Ftikos C (2007) Influence of A- and B-site doping on the properties of the system $La_2CoO_{4\pm\delta}$. J Eur Ceram Soc 27(2):571
4. Munnings C, Skinner S, Amow G, Whitfield P, Davidson I (2005) Oxygen transport in the LaNiCoO system. Solid State Ion 176(23–24):1895
5. Takahashi S, Nishimoto S, Matsuda M, Miyake M (2010) Electrode properties of the Ruddlesden-Popper series, $La_{n+1}Ni_nO_{3n+1}$ (n = 1, 2, and 3), as intermediate-temperature solid oxide fuel cells. J Am Ceram Soc 93(8):2329
6. Yashima M, Sirikanda N, Ishihara T (2010) Crystal structure, diffusion path, and oxygen permeability of a Pr_2NiO_4-based mixed conductor $(Pr_{0.9}La_{0.1})_2(Ni_{0.74}Cu_{0.21}Ga_{0.05})O_{4+\delta}$. J Am Chem Soc 132(7):2385
7. Lee D, Lee Y-L, Grimaud A, Hong WT, Biegalski MD, Morgan D, Shao-Horn Y (2014) Strontium influence on the oxygen electrocatalysis of $La_{2-x}Sr_xNiO_{4\pm\delta}$ $(0.0 \le x_{Sr} \le 1.0)$ thin films. J Mater Chem A 2:6480
8. Ishihara T, Sirikanda N, Nakashima K, Miyoshi S, Matsumoto H (2010) Mixed oxide ion and hole conductivity in $Pr_{2-\alpha}Ni_{0.76-x}Cu_{0.24}Ga_xO_{4+\delta}$ membrane. J Electrochem Soc 157(1):B141
9. Burriel M, Garcia G, Santiso J, Kilner JA, Chater RJ, Skinner SJ (2008) Anisotropic oxygen diffusion properties in epitaxial thin films of $La_2NiO_{4+\delta}$. J Mater Chem 18(4):416
10. Burriel M, Garcia G, Rossell MD, Figueras A, Van Tendeloo G, Santiso J (2007) Enhanced high-temperature electronic transport properties in nanostructured epitaxial thin films of

the $La_{n+1}Ni_nO_{3n+1}$ Ruddlesden−Popper series (n = 1, 2, 3, ∞). Chem Mater 19(16):4056
11. Boehm E, Bassat JM, Dordor P, Mauvy F, Grenier JC, Stevens P (2005) Oxygen diffusion and transport properties in non-stoichiometric $Ln_{2-x}NiO_{4+\delta}$ oxides. Solid State Ion 176(37–38):2717
12. Skinner SJ, Amow G (2007) Structural observations on $La_2(Ni,Co)O_{4\pm\delta}$ phases determined from in situ neutron powder diffraction. J Solid State Chem 180(7):1977
13. Huan Y, Chen S, Zeng R, Wei T, Dong D, Hu X, Huang Y (2019) Intrinsic effects of Ruddlesden-Popper-based bifunctional catalysts for high-temperature oxygen reduction and evolution. Adv Energy Mater 9:1901573
14. Munnings CN, Skinner SJ, Amow G, Whitfield PS, Davidson IJ (2005) Oxygen transport in the $La_2Ni_{1-x}Co_xO_{4+\delta}$ system. Solid State Ion 176(23):1895
15. Kharton VV, Yaremchenko AA, Shaula AL, Patrakeev MV, Naumovich EN, Logvinovich DI, Frade JR, Marques FMB (2004) Transport properties and stability of Ni-containing mixed conductors with perovskite- and K_2NiF_4-type structure. J Solid State Chem 177(1):26
16. Skinner SJ, Kilner JA (2000) Oxygen diffusion and surface exchange in $La_{2-x}Sr_xNiO_{4+\delta}$. Solid State Ion 135(1):709
17. Shen Y, Zhao H, Świerczek K, Du Z, Xie Z (2013) Lattice structure, sintering behavior and electrochemical performance of $La_{1.7}Ca_{0.3}Ni_{1-x}Cu_xO_{4+\delta}$ as cathode material for intermediate-temperature solid oxide fuel cell. J Power Sources 240:759
18. Tarancón A, Burriel M, Santiso J, Skinner SJ, Kilner JA (2010) Advances in layered oxide cathodes for intermediate temperature solid oxide fuel cells. J Mater Chem 20(19):3799
19. Huang X, Shin TH, Zhou J, Irvine JTS (2015) Hierarchically nanoporous $La_{1.7}Ca_{0.3}CuO_{4-\delta}$ and $La_{1.7}Ca_{0.3}Ni_xCu_{1-x}O_{4-\delta}$ ($0.25 \le x \le 0.75$) as potential cathode materials for IT-SOFCs. J Mater Chem A 3(25):13468
20. Skinner SJ (2001) Recent advances in perovskite-type materials for solid oxide fuel cell cathodes. Int J Inorg Mater 3(2):113
21. Adler SB (2004) Factors governing oxygen reduction in solid oxide fuel cell cathodes. Chem Rev 104(10):4791
22. Boehm E, Bassat JM, Steil MC, Dordor P, Mauvy F, Grenier JC (2003) Oxygen transport properties of $La_2Ni_{1-x}Cu_xO_{4+\delta}$ mixed conducting oxides. Solid State Sci 5(7):973
23. Boehm E, Bassat JM, Dordor P, Mauvy F, Grenier JC, Stevens P (2005) Oxygen diffusion and transport properties in non-stoichiometric $Ln_{2-x}NiO_{4+\delta}$ oxides. Solid State Ion 176(37):2717
24. Jeen H, Bi Z, Choi WS, Chisholm MF, Bridges CA, Paranthaman MP, Lee HN (2013) Orienting oxygen vacancies for fast catalytic reaction. Adv Mater 25(44):6459
25. Shao Z, Haile SM (2004) A high-performance cathode for the next generation of solid-oxide fuel cells. Nature 431(7005):170
26. Januschewsky J, Ahrens M, Opitz A, Kubel F, Fleig J (2009) Optimized $La_{0.6}Sr_{0.4}CoO_{3-\delta}$ thin-film electrodes with extremely fast oxygen-reduction kinetics. Adv Funct Mater 19(19):3151
27. Aguadero A, Pérez-Coll D, Alonso JA, Skinner SJ, Kilner J (2012) A new family of Mo-doped $SrCoO_{3-\delta}$ perovskites for application in reversible solid state electrochemical cells. Chem Mater 24(14):2655
28. Zhou W, Sunarso J, Chen Z-G, Ge L, Motuzas J, Zou J, Wang G, Julbe A, Zhu Z (2011) Novel B-site ordered double perovskite $Ba_2Bi_{0.1}Sc_{0.2}Co_{1.7}O_{6-x}$ for highly efficient oxygen reduction reaction. Energy Environ Sci 4(3):872
29. Zhou W, Sunarso J, Motuzas J, Liang F, Chen Z, Ge L, Liu S, Julbe A, Zhu Z (2011) Deactivation and regeneration of oxygen reduction reactivity on double perovskite $Ba_2Bi_{0.1}Sc_{0.2}Co_{1.7}O_{6-x}$ cathode for intermediate-temperature solid oxide fuel cells. Chem Mater 23(6):1618
30. Jiang L, Wei T, Zeng R, Zhang W-X, Huang Y-H (2013) Thermal and electrochemical properties of $PrBa_{0.5}Sr_{0.5}Co_{2-x}Fe_xO_{5+\delta}$ ($x = 0.5, 1.0, 1.5$) cathode materials for solid-oxide fuel cells. J Power Sources 232:279
31. Jacobson AJ (2010) Materials for solid oxide fuel cells. Chem Mater 22(3):660
32. Lee KT, Manthiram A (2006) Comparison of $Ln_{0.6}Sr_{0.4}CoO_{3-\delta}$ (Ln = La , Pr, Nd, Sm, and Gd) as cathode materials for intermediate temperature solid oxide fuel cells. J Electrochem Soc 153(4):794
33. Malavasi L, Fisher CAJ, Islam MS (2010) Oxide-ion and proton conducting electrolyte materials for clean energy applications: structural and mechanistic features. Chem Soc Rev 39(11):4370
34. Montenegro-Hernández A, Vega-Castillo J, Mogni L, Caneiro A (2011) Thermal stability of $Ln_2NiO_{4+\delta}$ (Ln: La, Pr, Nd) and their chemical compatibility with YSZ and CGO solid electrolytes. Int J Hydrogen Energy 36(24):15704
35. Al Daroukh M, Vashook VV, Ullmann H, Tietz F, Arual Raj I (2003) Oxides of the AMO_3 and A_2MO_4-type: structural stability, electrical conductivity and thermal expansion. Solid State Ionss 158(1):141
36. Wang Y, Nie H, Wang S, Wen T-L, Guth U, Valshook V (2006) $A_{2-\alpha}A'_\alpha BO_4$-type oxides as cathode materials for IT-SOFCs (A = Pr, Sm; A' = Sr; B = Fe, Co). Mater Lett 60(9):1174
37. Pérez-Coll D, Aguadero A (2011) Electrochemical performance of La_2NiO_4-based cathode for solid oxide fuel cells. Single Cell Test Fuel Cells 11(1):91
38. Burriel M, Wilkins S, Hill JP, Muñoz-Márquez MA, Brongersma HH, Kilner JA, Ryan MP, Skinner SJ (2014) Absence of Ni on the outer surface of Sr doped La_2NiO_4 single crystals. Energy Environ Sci 7(1):311
39. Hu Y, Bouffanais Y, Almar L, Morata A, Tarancon A, Dezanneau G (2013) $La_{2-x}Sr_xCoO_{4-\delta}$ ($x = 0.9, 1.0, 1.1$) Ruddlesden-Popper-type layered cobaltites as cathode materials for IT-SOFC application. Int J Hydrogen Energy 38(7):3064
40. Ghorbani-Moghadam T, Kompany A, Bagheri-Mohagheghi MM, Abrishami ME (2018) High temperature electrical conductivity and electrochemical investigation of $La_{2-x}Sr_xCoO_4$ nanoparticles for IT-SOFC cathode. Ceram Int 44(17):21238
41. Jin C, Liu J (2009) Preparation of $Ba_{1.2}Sr_{0.8}CoO_{4+\delta}$ K_2NiF_4-type structure oxide and cathodic behavioral of $Ba_{1.2}Sr_{0.8}CoO_{4+\delta}$–GDC composite cathode for intermediate temperature solid oxide fuel cells. J Alloys Compd 474(1):573
42. Zhou J, Chen G, Wu K, Cheng Y (2013) $La_{0.8}Sr_{1.2}CoO_{4+\delta}$–CGO composite as cathode on $La_{0.9}Sr_{0.1}Ga_{0.8}Mg_{0.2}O_{3-\delta}$ electrolyte for intermediate temperature solid oxide fuel cells. J Power Sources 232:332
43. Tealdi C, Ferrara C, Mustarelli P, Islam MS (2012) Vacancy and interstitial oxide ion migration in heavily doped $La_{2-x}Sr_xCoO_{4\pm\delta}$. J Mater Chem 22:8969
44. Huang YH, Dass RI, Xing ZL, Goodenough JB (2006) Double perovskites as anode materials for solid-oxide fuel cells. Science 312(5771):254
45. Huang Y-H, Liang G, Croft M, Lehtimäki M, Karppinen M, Goodenough JB (2009) Double-perovskite anode materials Sr_2MMoO_6 (M = Co, Ni) for solid oxide fuel cells. Chem Mater 21(11):2319
46. Li F, Jiang L, Zeng R, Wei T, Wang F, Xu Y, Huang Y (2015) One-pot synthesized hetero-structured $Ca_3Co_2O6/La_{0.6}Ca_{0.4}CoO_3$ dual-phase composite cathode materials for solid-oxide fuel cells. Int J Hydrogen Energy 40(37):12750
47. Li F, Xia S, Xu Y, Yan Y, Sun C, Jiang L, Huang Y (2018) $Ca_3Co_2O_6$–$Ce_{0.8}Sm_{0.2}O_{1.9}$ composite cathode material for solid oxide fuel cells. J Alloys Compd 753:292

48. Jiang L, Liang G, Han J, Huang Y (2014) Effects of Sr-site deficiency on structure and electrochemical performance in Sr_2MgMoO_6 for solid-oxide fuel cell. J Power Sources 270:441
49. Ahad A, Shukla DK, Rahman F, Majid S, Tarachand OGS, Sinha AK, Phase DM (2017) Colossal thermopower, spin states and delocalization effects in single layered $La_{2-x}Sr_xCoO_4$. Acta Mater 135:233
50. Saitoh T, Mizokawa T, Fujimori A, Takeda Y, Takano M (1996) Electronic structure and magnetism in valence-control $La_{1-x}Sr_xCoO_3$. J Electron Spectrosc Relat Phenom 78:195
51. Dong ST, Sun N, Zhang BB, Zhang F, Yao SH, Zhou J, Zhang ST, Gu ZB, Chen YB, Chen YF (2015) Crystal growth, structure, and dielectric properties of layered cobaltates $La_{2-x}Sr_xCoO_4$ ($x = 0.4$, 0.5, and 0.6) single crystal. Mater Res Bull 61:352
52. Liu G, Li J, Yang K, Tang W, Liu H, Yang J, Yue R, Chen Y (2015) Effects of cerium incorporation on the catalytic oxidation of benzene over flame-made perovskite $La_{1-x}Ce_xMnO_3$ catalysts. Particuology 19:60
53. Falcón H, Barbero JA, Araujo G, Casais MT, Martínez-Lope MJ, Alonso JA, Fierro JLG (2004) Double perovskite oxides $A_2FeMoO_{6-\delta}$ (A = Ca, Sr and Ba) as catalysts for methane combustion. Appl Catal B 53(1):37
54. Zobel C, Kriener M, Bruns D, Baier J, Grüninger M, Lorenz T, Reutler P, Revcolevschi A (2002) Evidence for a low-spin to intermediate-spin state transition in $LaCoO_3$. Phys Rev B 66(2):020402
55. Ang R, Sun YP, Luo X, Hao CY, Song WH (2008) Studies of structural, magnetic, electrical and thermal properties in layered perovskite cobaltite $SrLnCoO_4$(Ln = La, Ce, Pr, Nd, Eu, Gd and Tb). J Phys D 41(4):045404